PHYSICAL REVIEW B VOLUME 14, NUMBER 12 15 DECEMBER 1976

Brillouin scattering from isotropic metals

Jan G. Dil* and Edward M. Brody
The Institute of Optics, University of Rochester, Rochester, New York 14627
(Received 24 July 1975; revised manuscript received 18 March 1976)

Brillouin scattering from isotropic metals is investigated experimentally and theoretically. The observation of highly asymmetric Brillouin spectra from liquid mercury and liquid gallium is reported. A comparison is made between theory and experiment; the theory includes the damping of the acoustic phonons. It is found that the present state of the theory only qualitatively describes the Brillouin scattering of light from highly opaque materials. The velocities of sound of mercury and gallium deduced from the measurements are found to be 38% larger than the corresponding values determined by ultrasonic techniques. The observed intensity is at least an order of magnitude larger than the theory predicts, and the line shape, especially in the case of liquid gallium, differs appreciably from the theoretical line shape. The major origin of the discrepancy between theory and experiment is believed to be the simple model employed for the description of the dynamics of the density fluctuations near the surface. The spectra observed may therefore contribute to further understanding of the surface physics of liquid metals.

I. INTRODUCTION

In 1971, the first prediction of the intensity and spectrum of light inelastically scattered from the long-wavelength acoustic modes in metallic and semiconducting crystals was made.[1,2] In these articles, it was shown that when the extinction index of the scatterer becomes as large as, or even larger than, the refractive index, the Brillouin spectra become highly asymmetric, exhibiting a sharp cutoff frequency followed by a long tail. It is the purpose of the present paper to investigate the experimental observation of these rather unusual Brillouin spectra. Brillouin-scattering measurements from the metals liquid mercury and liquid gallium are reported showing the asymmetric line shape.

During 1970–1972, Sandercock[3-5] made the first successful Brillouin-scattering measurements on nontransparent semiconductors. By using a multiple-pass Fabry-Perot interferometer, he achieved a trememdous increase in contrast which meant that the large amount of elastically scattered light arising from surface defects, which completely swamps the much weaker Brillouin components, could be rejected. The spectra he observed from the semiconductors were broad Lorentzians in agreement with the theory he presented in which the approximation was made that the extinction index was small compared to the refractive index.

Our experimental approach was to assemble a spectrometer similar to the one designed by Sandercock.[4,5] The contrast of our five-pass Fabry-Perot interferometer was in excess of 10^{12} so that the large amount of diffuse elastic scattering from the surface could be rejected. In addition, it was found necessary to clean the sample surfaces and keep them under vacuum. A description of the present interferometer and sample preparation is given in Sec. II of this paper.

Section III contains a concise description of the theory of Brillouin scattering from a general nontransparent isotropic material, in particular from a liquid metal. The damping of the thermal phonons has been included. Moreover, the scattering from the isobaric density fluctuations in a nontransparent medium is treated.

Section IV contains our spectral data from mercury and gallium, and, finally, Sec. V deals with a comparison of these data with the theory presented in Sec. III.

The mks system of Giorgi is employed throughout this paper.

II. EXPERIMENTAL APPROACH

A. Brillouin spectrometer

A Brillouin spectrometer is used to measure the power, the spectral composition, and the polarization of monochromatic light inelastically scattered from a sample. With regard to the spectral composition of the inelastically scattered light, Brillouin spectroscopy is somewhat arbitrarily confined to a frequency band between 150 MHz–500 GHz, i.e., 0.005–16 cm^{-1} around the frequency, $\nu_0 \simeq 6\times10^{14}$ Hz, of the incident light. It should be clear that the Fabry-Perot interferometer is ideal for resolving this frequency band.

Let us consider the flow diagram of the spectrometer as depicted in Fig. 1. The spectrometer has many similarities to the one of Sandercock.[4,5] A laser beam is focused by the lens l_1 on a sample which is a highly reflective metal surface. Through an interaction process, some of this incident light is scattered inelastically and collected by the lens l_2. In order to unambiguously define the scattering volume in the sample, a spatial filter consisting of the two confocal lenses l_3 and l_4, and a pinhole p_1 is introduced. Between this spatial filter and the collecting lens, a polarization analyzer P and an aperture A_1 to limit the beam diameter are inserted. The beam of parallel light leaving the spatial filter contains mainly light elastically scattered from surface imperfections or impurities. The tiny signal in which we are interested is filtered out from this elastically scattered light by the piezoelectrically scanned plane Fabry-Perot interferometer. The contrast and finesse of this instrument are drastically improved by routing the transmitted beam sequentially through five different portions of the interferometer mirrors. This is accomplished by means of the two prisms, pr_1 and pr_2.

In order to ensure that the contrast of the multiple-pass instrument is not affected by the divergence of the beam leaving the spatial filter, the focal length f of l_3 and l_4, and the diameter p_1 have to be chosen in such a way that

$$p_1/2f \ll (\lambda_0/2dN_1)^{1/2}. \tag{2.1}$$

In Eq. (2.1), λ_0 is the wavelength of the incident light, d is the distance between the interferometer plates, and N_1 is the measured single-pass finesse.

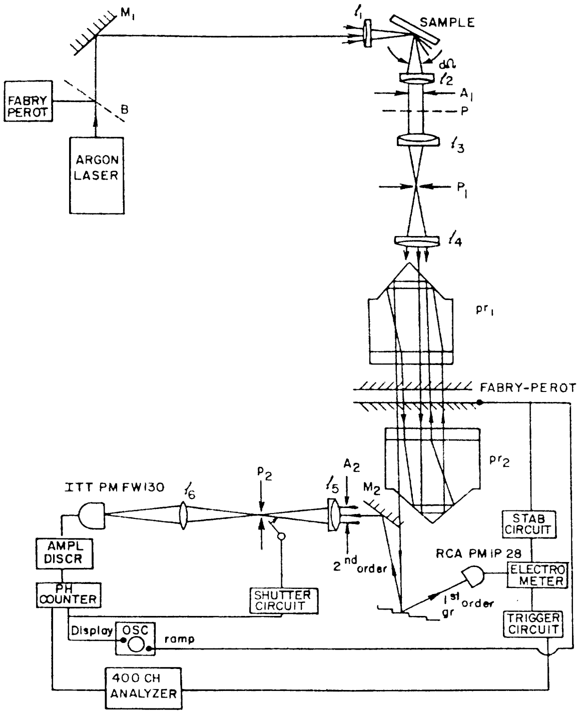

FIG. 1. Brillouin spectrometer. M_1 and M_2 are mirrors; l_1-l_6 are lenses, A_1 and A_2 are apertures; P is a polarizer; p_1 and p_2 are pinholes; pr_1 and pr_2 are prisms; gr is a grating.

The focal lengths of l_1 and l_2 are then determined by the condition that the incident focal spot on the sample has to be imaged right on or inside p_1.

The light beam leaving the interferometer is incident on the grating gr, which diffracts strongly in the second order all the light whose frequencies lie within a range which is determined by the pinhole p_2 and the lens l_5. This discriminates against larger shifts which may show up due to fluorescence or Raman scattering. The pinhole p_2 is reimaged on the sensitive area of the photomultiplier by the lens l_6.

The electrical signal leaving the photomultiplier is discriminated, amplified, and then fed into a photon counter. Its digital output is recorded on a 400-channel analyzer.

The Fabry-Perot interferometer is scanned by using the ramp voltage of the display oscilloscope. Each scan is 5 sec. The resulting signals are added on the 400-channel analyzer. Each sweep of the 400-channel analyzer begins at a fixed delay from the center of the first peak which shows up at the beginning of each scan when the interferometer is on resonance at the frequency of the incident light. The limiting noise is the dark count rate of the photomultiplier. An ITT FW130 tube is used having a 0.36-mm-diam photocathode. Uncooled, its dark count rate is $\frac{1}{3}$ count per second.

The weakly diffracted first-order signal from the grating is detected by an insensitive photomultiplier and used to actuate the start of the sweep of the 400-channel analyzer. It also serves to stabilize the interferometer by means of an electronic servo system.

A shutter between p_2 and l_5 can be activated for an adjustable time interval whenever the photon count rate exceeds a preset value, thus preventing saturation of the photomultiplier.

The optical part of the spectrometer is mounted on a vibration-isolated table. The mechanical stability of this table must be such that the image of the focal spot at the sample never misses the pinholes.

The total efficiency η of the spectrometer can be defined as the ratio of the number of counts/sec recorded by the photon counter and the number of photons/sec leaving the lens l_4. The efficiency was calibrated in a scattering measurement on methanol. The contrast is the ratio of the maximum transmission of the interferometer on resonance to its minimum transmission at antiresonance for monochromatic radiation. By suitably attenuating the input signal on resonance, and removing the attenuation off resonance, it was possible to make direct contrast measurements using the photon counter. The values of η, together with the experimentally determined values of the five pass contrast, C_5, and the five pass finesse, N_5, of the interferometer are collected in Table I for the two strong lines of the Ar-ion laser. The variation of C_5, N_5, and η with λ_0 result from the fact that the reflectivity of the interferometer mirrors also depends on λ_0. For a detailed description of the interferometer, the reader is referred to Ref. 6, Chap. 3.

B. Sample preparation

We concentrated on liquid metals which were readily available. Triply distilled mercury was purchased; the gallium obtained was specified to be 99.999 99% pure. As our initial measurements on mercury and gallium surfaces exposed to air indicated surface contamination,[6] a cell was designed to allow removal of adsorbed surface films (Fig. 2).

The cleaning procedure for the liquid-metal surfaces was similar to the one Faber and Smith[7] applied to their ellipsometric measurements on liquid metals. After the cell is evacuated, helium is admitted and the surface is cleaned in a glow discharge. The discharge occurs at a pressure of ≃0.5 Torr and when ≃700 V is applied between the anode and the cathode. After the discharge, the cell is reevacuated, and the pressure is kept well below 10^{-4} Torr by an oil diffusion pump with a liquid nitrogen trap. Faber and Smith[7] showed that at this pressure the surface remained clean.

III. THEORETICAL APPROACH

In this section, expressions for the smoothed energy spectrum of light inelastically scattered from the acoustic density fluctuations in isotropic nontransparent media are given. Emphasis is placed on the physics of the scattering process and the assumptions which are made to arrive at the final formulas. This is done to clarify the discrepancies which appear between theory and experiment. The details of the derivations can be found elsewhere.[6,8] The correspondence or disagreement with earlier calculations is noted where pertinent.

The analysis of Brillouin scattering from nontransparent media may be separated into three topics. First, the mechanism by which the incident light couples to the density fluctuations has to be constructed. Second, the incident light penetrates a shallow depth into the scatterer. Hence, the electromagnetic boundary condition problem of a localized source embedded in the scatterer just below a planar interface and radiating into the vacuum above that interface has to be solved. Third, the dynamics of the density fluctuations appropriate to the scattering volume must be employed.

TABLE I. Five-pass contrast C_5, five-pass finesse N_5, and efficiency η of the present spectrometer.

λ_0 [nm]	C_5	N_5	η (counts/photon)
488	$\simeq 10^{10}$	45 ± 5	0.33%
514.5	$>10^{12}$	90 ± 10	0.15%

In regard to the first topic, the coupling mechanism, it is convenient to consider the effects of the bound and free electrons separately. The thermodynamic density fluctuations modulate the permittivity which pertains to the response of the bound electrons, and the electrical conductivity which pertains to the response of the free electrons. In the case of transparent materials or highly polarizable semiconductors such as silicon and germanium, the coupling between the permittivity and the density is determined by the creation of dipoles and governed by the Lorentz-Lorenz relation. For such materials, the electrical conductivity can be neglected at optical frequencies. However, for the case of liquid metals, the optical constants are predominantly determined by the electrical conductivity $\sigma(\omega)$,[9] as may be expressed by the Drude formula

$$\sigma(\omega) = \frac{N_e e^2/m_e}{\tau_D^{-1} - i\omega} \equiv \frac{\omega\epsilon_0}{i}\{[n(\omega) + i\kappa(\omega)]^2 - 1\}, \tag{3.1}$$

where the permittivity is set equal to $\epsilon_0 = (1/36\pi) \times 10^{-9}$ F/m. In Eq. (3.1), ω denotes an angular frequency, N_e is the density of free electrons,

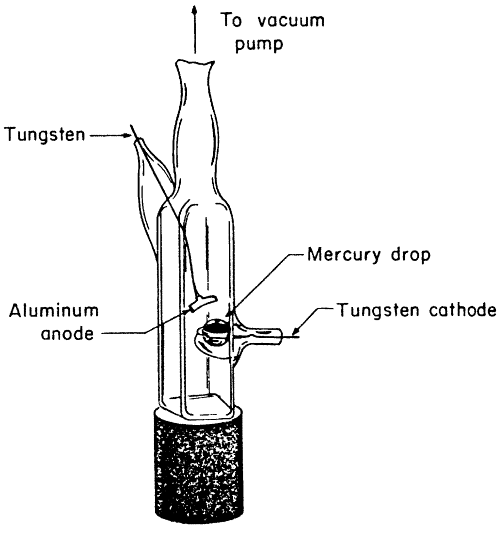

FIG. 2. Sample cell.

e and m_e are the electronic charge and mass, τ_D is the Drude relaxation time, and $n(\omega)$ and $\kappa(\omega)$ are the refractive and extinction indices.

According to Spector,[10] for longitudinal ionic displacements in metals, charge neutrality is maintained through purely electromagnetic coupling between the ions and the free electrons up to frequencies approaching the plasma frequency. In other words, the free electrons instantaneously follow the longitudinal ionic displacements. Therefore, the fluctuations in the density of ions ρ modulate the electrical conductivity as

$$\rho \frac{\partial \sigma(\omega)}{\partial \rho} = N_e \frac{\partial \sigma(\omega)}{\partial N_e} . \tag{3.2a}$$

As can be seen from Eq. (3.1)

$$N_e \frac{\partial \sigma(\omega)}{\partial N_e} = \sigma(\omega) . \tag{3.2b}$$

Consequently, Brillouin scattering from liquid metals is light scattering from the free electrons. The density fluctuations produce an excess current density, $\Delta\vec{J}(\vec{r}, \omega_s)$, which can be expressed as

$$\Delta\vec{J}(\vec{r}, \omega_s) = \Delta\sigma(\vec{r}; \omega_s, \omega_0)\vec{E}_0(\vec{r}, \omega_0) , \tag{3.3}$$

where $\vec{E}_0(\vec{r}, \omega_0)$ stands for the given incident electric field inside the scatterer with angular frequency ω_0, and ω_s denotes the angular frequency of the inelastically scattered field.

The second topic, the radiation of a source across a plane, arises from the experimental conditions. The incident laser beam is focused to a small spot at the metal-vacuum interface and penetrates only a few hundred angstroms into liquid mercury or gallium. In a backscattering geometry, the emerging inelastically scattered light is collected at the point P of observation (Fig. 3). Since P is many wavelengths of light distant from the focal spot and outside the scatterer, and since the scattering volume subtends a very small solid angle with respect to P, we need to find the far-field solutions for the electromagnetic field vectors, $\vec{E}_s(\vec{r}_p, \omega_s)$ and $\vec{H}_s(\vec{r}_p, \omega_s)$, scattered from the density fluctuations. These field vectors are determined by the Maxwell equations with the source term of Eq. (3.3).

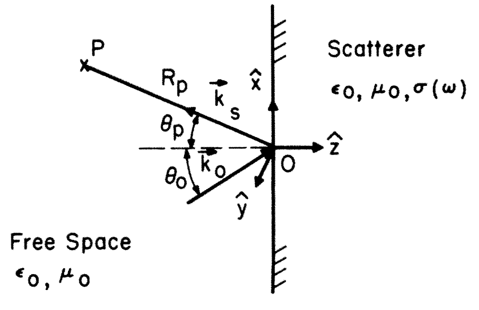

FIG. 3. Scattering geometry. The sample surface is the xy plane; ϵ_0, μ_0, and $\sigma(\omega)$ stand for permittivity, permeability, and conductivity; P is the point of observation; θ_0 and θ_p are the angles of incidence and observation; $\vec{k}_0$ and $\vec{k}_s$ are the wave vectors of the incident and scattered light outside the metal; R_p is the distance between P and O, the focus of the incident laser beam.

The solution to the resulting electromagnetic-boundary-condition problem may be obtained in various ways. Our approach is to decompose both the source and the far field into vector components parallel and perpendicular to the plane of observation. This decomposition was first introduced by Gasper *et al.*[11,12] and applied by Dil[6,8] to the problem of Brillouin scattering from metals. The advantage of this approach is that the transfer coefficients connecting the fields inside and outside the scatterer are the familiar Fresnel coefficients multiplied by a divergence factor. This factor accounts for the difference in divergence of the fields inside and outside the scatterer. Our formulas simplify if we consider materials for which

$$|n(\omega) - \kappa(\omega)| \gg \frac{\sin^2(\theta)}{n(\omega) + \kappa(\omega)} , \tag{3.4}$$

where θ is either the angle of incidence θ_0, or the angle of observation θ_p. This condition is fulfilled by most semiconductors and liquid metals. When Eq. (3.4) holds, the scattered far field can be written[6,8]

$$\vec{E}_s(\vec{r}_p, \omega_s) = \vec{G}(\vec{r}_p; \omega_s; \vec{e}_0) \times \sum_{q_z=0}^{\infty} \frac{-\Delta\sigma_q(\omega_s, \omega_0)}{i(q_z - 2nk_s) + 2\kappa k_s} . \tag{3.5}$$

In Eq. (3.5), the optical constants are evaluated at ω_s ignoring the dispersion over the frequency interval $[\omega_0, \omega_s]$, and the propagation constants of the incident and scattered fields outside the scatterer are set equal to k_s. The vector $\vec{G}(\vec{r}_p; \omega_s; \vec{e}_0)$, in Eq. (3.5) can be expressed

$$\vec{G}(\vec{r}_p; \omega_s; \vec{e}_0) \equiv i\omega_s \mu_0 (t_\parallel e_{0\parallel} \hat{i}_\parallel + t_\perp e_{0\perp} \hat{i}_\perp) \times \frac{\cos(\theta_p)}{n + i\kappa} \frac{e^{ik_s R_p}}{4\pi R_p} S_i , \tag{3.6}$$

in which $\mu_0 = 4\pi \times 10^{-7}$ H/m denotes the permeability of free space,

$$k_s \equiv \omega_s (\epsilon_0 \mu_0)^{1/2} , \tag{3.7}$$

is the propagation constant of the scattered wave outside the scatterer, R_p is the distance between P and the source, and S_i is the area of the incident laser beam focused onto the scatterer (Fig. 3). Inspection of Eq. (3.6) shows that it contains two vector components, one parallel $\hat{i}_\parallel$ and one perpendicular $\hat{i}_\perp$ to the plane of observation. The source term of Eq. (3.3) is proportional to the given incident electric field just across the boundary inside the scatterer

$$\vec{e}_0 \equiv \vec{E}_0(\vec{r}=0^+, \omega_0), \tag{3.8}$$

which is also decomposed into components parallel $e_{0\parallel}$ and perpendicular $e_{0\perp}$ to the plane of observation. Under the assumption of Eq. (3.4), $e_{0\parallel}$ is the component of $\vec{e}_0$ parallel to the interface. The electromagnetic fields radiated by this source are transferred across the boundary by the familiar Fresnel coefficients

$$\begin{aligned} t_\parallel &= \frac{2(n+i\kappa)}{1+(n+i\kappa)\cos(\theta_p)}, \\ t_\perp &= \frac{2(n+i\kappa)}{n+i\kappa+\cos(\theta_p)}, \end{aligned} \tag{3.9}$$

multiplied by the divergence factor $\cos(\theta_p)/(n+i\kappa)$. Note that the formulas given here only hold when Eq. (3.4) is applicable.

The expression for the scattered electric far field given by Eq. (3.5) is equivalent with the corresponding expression in the transparent case given by Fabelinskii [Ref. 13, Eqs. (1.20)–(1.22)]. In this latter case $\kappa=0$ and the denominator in Eq. (3.5) reduces to a resonant term so that only $q_z = 2nk_s$ contributes to the summation. Here, q denote the propagation constants in the spatial Fourier expansion of $\Delta\sigma(\vec{r})$,

$$q \equiv (q_\pi^2 + q_z^2)^{1/2}, \tag{3.10}$$

where q_π is the component of q parallel to the surface,

$$q_\pi = k_s[\sin(\theta_0) - \sin(\theta_p)], \tag{3.11}$$

which is determined by the scattering geometry (Fig. 3). The fixed value of q_π reflects the fact that the components of the electromagnetic field vectors parallel to the scattering surface are conserved across the boundary. For nontransparent scatterers ($\kappa \neq 0$), Eq. (3.5) shows that in a range $0 \leq |q_z| \lesssim 2\kappa k_s$ there are contributions to the scattering process reflecting the spatial decay of both the incident and the scattered wave.

At this point it is appropriate to compare the formulas presented here with the corresponding expressions given in previous work. When the planes of incidence and observation are chosen to coincide with the *xz* plane, and when the incident electric field is polarized parallel to the *y* axis, examination of Eqs. (3.5)–(3.9) shows that the factor $2k_s\cos(\theta_p)S_i/4\pi R_p$ is missing in the Mills *et al.* formulas [Ref. 14, Eqs. (2.12)–(2.13)]. This discrepancy arises because these authors did not perform the asymptotic expansion appropriate for the far-field integral expression for $\vec{E}_s(\vec{r}_p, \omega_s)$. It is this expansion which leads to the R_p^{-1} dependence of the field vectors and to the divergence factor. The detailed derivation of our expressions can be found in Refs. 6 and 8, where more general cases are treated.

The quantity of experimental interest is the energy arriving at the point of observation per unit area and per unit frequency interval. This quantity equals the smoothed theoretical energy spectrum $S(\vec{r}_p, \omega_s)$ of the scattered wave and is defined by[15]

$$S(\vec{r}_p, \omega_s) \equiv (1/\pi)(\epsilon_0/\mu_0)^{1/2}|\vec{E}_s(\vec{r}_p, \omega_s)|^2. \tag{3.12}$$

Before substituting Eq. (3.5) in Eq. (3.12), we note that through the assumption of purely electromagnetic coupling between the fluctuating density of ions and the free electrons [Eq. (3.2)], the coefficients of the spatial Fourier expansion of $\Delta\sigma(\vec{r}; \omega_s, \omega_0)$ can be rewritten

$$\Delta\sigma_q(\omega_s, \omega_0) = \frac{\partial\sigma(\omega_0)}{\partial\rho}\Delta\rho_q(\omega_s - \omega_0). \tag{3.13a}$$

Using Eqs. (3.1) and (3.2) we find

$$\frac{\partial\sigma(\omega_0)}{\partial\rho} = \frac{(n+i\kappa)^2 - 1}{\rho}\,\frac{\omega_0\epsilon_0}{i}, \tag{3.13b}$$

so that after substitution in Eq. (3.5), Eq. (3.12) reduces to

$$\begin{aligned} S(\vec{r}_p, \omega_s) = {} & \frac{1}{\pi}\left(\frac{\epsilon_0}{\mu_0}\right)^{1/2} |\vec{G}(\vec{r}_p; \omega_s; \vec{e}_0)|^2 \frac{|(n+i\kappa)^2 - 1|^2}{\rho^2} \\ & \times \sum_{q_z=0}^{\infty} \frac{\langle|\Delta\rho_q(\omega_s - \omega_0)|^2\rangle}{(q_z - 2nk_s)^2 + (2\kappa k_s)^2}. \end{aligned} \tag{3.14}$$

Equation (3.14) leads to the third topic, that of the dynamics of the random density fluctuations. The smoothed energy spectrum of the density fluctuations, $\langle|\Delta\rho_q(\omega_s - \omega_0)|^2\rangle$, in a region very close to a surface (a few hundred angstroms) may well be affected by the presence of this interface. However, a first calculation for this energy spectrum can be obtained from the small signal acoustic equations which hold for an infinite continuum. Using these equations, it is shown in Ref. 6 that

$$\begin{aligned} \langle|\Delta\rho_q(\omega_s - \omega_0)|^2\rangle = {} & \pi\frac{\beta_S kT}{V_i}\rho^2\tau\tfrac{1}{2}[\mathcal{L}(\omega_s - \omega_0 - \Omega_{\text{ad}}(q); \gamma_{\text{ad}}(q)) + \mathcal{L}(\omega_s - \omega_0 + \Omega_{\text{ad}}(q); \gamma_{\text{ad}}(q))] \\ & + \pi\frac{(\beta_T - \beta_S)kT}{V_i}\rho^2\tau\mathcal{L}(\omega_s - \omega_0; \gamma_{\text{is}}(q)), \end{aligned} \tag{3.15}$$

where $\beta_{S,T}$ denotes the adiabatic, or isothermal, compressibility, k denotes Boltzmann's constant, T is the absolute temperature, V_i is the interaction volume, τ is the time of observation, and

$$\mathcal{L}(\omega;\gamma_l)\equiv(\gamma_l/2\pi)/(\omega^2+\tfrac{1}{4}\gamma_l^2) \qquad (3.16)$$

denotes the normalized Lorentz function. The time of observation appears explicitly in Eq. (3.15) because the smoothing process is an integration over time. To get the time average, both sides must be divided by τ and that is the more common form for the expression.

The first two Lorentzians in Eq. (3.15) are the anti-Stokes and the Stokes components, respectively, which are a result of scattering from thermal sound waves traveling in opposite directions. The last Lorentzian originates with the scattering from nonpropagating diffusive heat waves. For values of q such that

$$q\lesssim v/\chi\,, \qquad (3.17)$$

v being the velocity of sound and χ denoting the thermal diffusivity, the angular frequency and the inverse relaxation times of the adiabatic and isobaric density fluctuations are given by their long-wavelength limits, i.e.,

$$\Omega_{\text{ad}}(q)=vq,\quad \gamma_{\text{ad}}(q)=\Gamma q^2,\quad \gamma_{\text{is}}(q)=2\chi q^2\,, \qquad (3.18)$$

where Γ is a damping coefficient.

The line shape of the energy spectrum is determined by the summation in Eq. (3.14), where each term is a Lorentzian as given by Eq. (3.15) divided by a weighting function. The summation in Eq. (3.14) can be evaluated numerically or analytically by conversion into an integral. The result of this conversion into an integral is given in the Appendix.

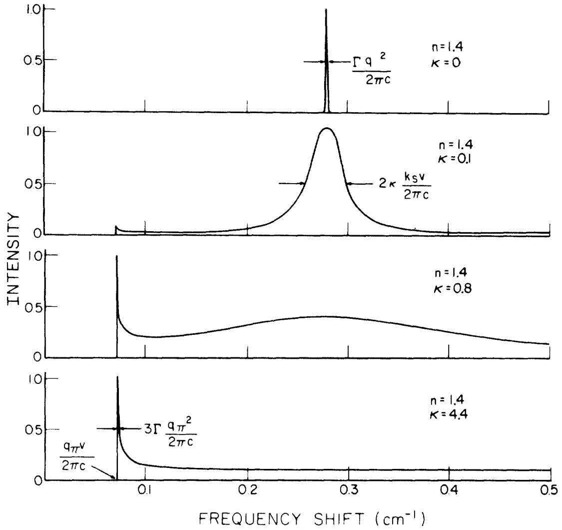

FIG. 4. Brillouin line shapes for materials of increasing opacity. The optical constants, n and κ, of the bottom curve pertain to liquid mercury (Ref. 7); c is the velocity of light with propagation constant k_S; v is the velocity of sound with damping Γ and propagation constant q; q_π is the component of q parallel to the surface.

The resulting line shapes for the anti-Stokes component are illustrated in Fig. 4 for different values of the extinction index κ. It can be concluded from these theoretical spectra that when the scatterer becomes more opaque, the Brillouin spectra first form broad symmetric Lorentzians as was pointed out by Sandercock.[4] These spectra do not contain observable information about the damping of the phonons. When κ becomes larger than n, as is the case for liquid mercury and gallium, the spectra become highly asymmetric showing a sharp onset frequency when $q=q_\pi$. This cutoff frequency reflects the conservation of the wave vectors parallel to the interface. The line shape of the spectrum around this cutoff frequency is given by $f(\delta)$ in Eq. (A5) and does contain direct information about the velocity and the damping of the phonons. The spectrum after the cutoff frequency decreases as

$$f(\delta)=\frac{1}{\sqrt{2}\,\delta^{1/2}}=\frac{1}{\{1-[q_\pi v/(\omega_s-\omega_0)]^2\}^{1/2}}$$
$$\text{for } \omega_s-\omega_0-q_\pi v\gg\Gamma q_\pi^2\,, \qquad (3.19)$$

a result that was derived earlier by Bennett *et al.*[2] For frequencies $\omega_s-\omega_0\gg q_\pi v$ the spectrum decreases to zero according to the function given by Eq. (A2a). This long tail, beginning at roughly 0.1 cm^{-1} for the case $n=1.4$ and $\kappa=4.4$ in Fig. 4, reflects the participation of all q_z components for which $0\leq q_z\lesssim 2\kappa k_S$ in the scattering process. All these components participate because both the incident and the inelastically scattered wave contain a range of spatial Fourier components perpendicular to the interface.

It should be clear that the Stokes component $I_S(\omega_0-\omega_s)$ in the Brillouin spectra is given by

$$I_S(\omega_0-\omega_s)=I_{AS}(\omega_s-\omega_0)\,. \qquad (3.20)$$

In Sec. IV we discuss the observation of these highly asymmetric Brillouin spectra from nontransparent media.

IV. DATA ACQUISITION AND ANALYSIS

A. Data acquisition

Once the liquid-metal surfaces were cleaned in a glow discharge, there were two major problems in taking the measurements. The first problem was to obtain a quiescent surface, a problem which was especially difficult with mercury.

The second problem was the imaging of the focal spot on the pinhole p_1 by the collecting lens l_2 (Fig. 1). Since the liquid-metal surfaces were so clean and smooth, they acted as ideal mirrors, and it was difficult to locate the exact position of the focal spot of the incident laser beam on the metal. In order to recognize the real focal spot in a background of many extraneous reflections, a microscope was focused on the pinhole p_1. By changing the position of the collecting lens l_2, and viewing through the microscope, the very weak but distinct focal spot could be imaged on p_1.

The mercury was held at room temperature, $T_{Hg} \simeq 297$ K; the temperature of the gallium was maintained at $T_{Ga} \simeq 378$ K, well above its melting temperature of 302 K. The power of the incident laser was between 200 and 300 mW, a power low enough to prevent surface distortion due to heating. When the laser beam was focused on the sample, the temperature of the bulk increased an additional 2 K.

Scattering measurements were performed with the 514.5-nm argon-ion laser line polarized either in the plane of incidence or perpendicular to it, either case giving spectra of equal quality. As mentioned before, the plane of incidence was arranged to coincide with the plane of observation. The scattering geometry was such that the wave vector of the incident light $\vec{k}_0$ was perpendicular to the direction of observation, given by $\vec{k}_s$. The instability of the mercury surface prevented longer accumulation times than 1 h. For gallium the accumulation time was typically 2 h.

B. Data analysis

Typical Brillouin spectra taken from liquid mercury and liquid gallium are shown in Fig. 5. Each dot represents the accumulated number of photoelectrons in one channel of the 400-channel analyzer. Each channel corresponds to an identical frequency interval, the size of which is the ratio of the free spectral range of the interferometer and the total number of channels between two successive maxima. These maxima define two zero-frequency shifts in Fig. 5 corresponding to the resonant transmission at the laser frequency of two successive orders of the interferometer. This large amount of scattering is due to diffuse reflection at the metal surface. The interval to the right of the first maximum corresponds to a positive frequency anti-Stokes shift, and the interval to the left corresponds to a negative frequency Stokes shift. Note that frequencies which differ by an integral multiple of the free spectral range are transmitted simultaneously. Therefore, the signal in the center interval of the observed spectra is the result of the buildup of scattered signals of overlapping orders.

Since the signals are weak, there is a large spread in the data points due to the Poisson distribution of the photoelectrons. Therefore, the data must be smoothed. We accomplished this using the Fortran scientific subroutine ICSSMU which is designed to smooth Poisson noise. The shaded areas in Fig. 5 are the regions within one standard deviation of this smoothed curve. The solid line is the theoretical line shape as determined by Eqs. (A2)–(A5) convolved with the instrumental profile.

One can see a similarity of features between the shaded areas and the solid curves. The onset frequencies are apparent as are definite asymmetries in the observed spectral line shapes. A detailed comparison with theory is discussed

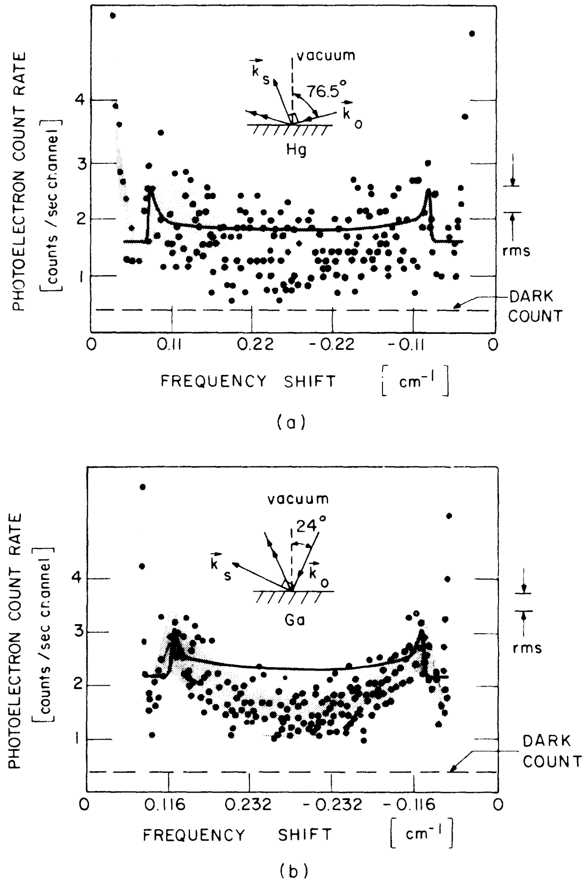

FIG. 5. Brillouin spectra from liquid mercury (a) and gallium (b); the free spectral range for Hg is 0.55 cm^{-1} = 392 channels; the free spectral range for Ga is 0.579 cm^{-1} = 400 channels. The ordinate is the absolute photoelectron count rate. The dots are the accumulated signal. The shaded area is the region within one standard deviation of a smoothed curve through the data points. The solid line is the theoretical line shape [Eqs. (A2)–(A6)] convolved with the instrumental profile.

in Sec. V.

The peaks following the onset frequencies could be located with a ±10% accuracy. According to Eq. (3.11), they occur when

$$q = q_\pi = k_s[\sin(\theta_0) - \sin(\theta_p)]$$
$$= k_s[\sin(\theta_0) - \cos(\theta_0)], \quad (4.1)$$

and are independent of the optical constants n and κ. By determining the frequency shifts Ω_{ad} at the peaks and taking spectra with a different angle of incidence θ_0 the $\Omega_{ad} = \Omega_{ad}(q_\pi)$ curves could be deduced. They are plotted in Fig. 6. In this way, within the experimental errors, a linear relation, $\Omega_{ad} = vq_\pi$, was inferred leading to velocities of sound $v_{Hg} = (1.9 \pm 0.4) \times 10^3$ m/sec and $v_{Ga} = (3.7 \pm 0.4) \times 10^3$ m/sec.

Scattering measurements on liquid gallium previously reported by the present authors[6,16] indicated a lower velocity of sound. The gallium used in these former measurements was later analyzed to be contaminated with mercury.

V. COMPARISON BETWEEN THEORY AND EXPERIMENT

The theory presented in Sec. III ought to be tested in four ways: (i) The polarization of the inelastically scattered light, (ii) the cutoff frequency, (iii) the energy per unit frequency interval, and (iv) the line shape.

The polarization dependence is determined by the Green's function of Eq. (3.6). It is of a vectorial rather than a tensorial form. As was pointed out in Sec. III, it contains two vector components, one parallel and one perpendicular to the plane of observation. For this reason, when it is substituted to Eq. (3.14), it leads only to polarized scattering, with no depolarized component. When the incident light was polarized perpendicular to the plane of observation, the inelastically scattered light was also totally polarized in this direction. Within the condition of Eq. (3.4), the complex wave vectors of the incident and scattered wave inside the metal are directed parallel to the z axis so that spectra should appear when the incident light is polarized parallel to the plane of observation. This was experimentally verified.

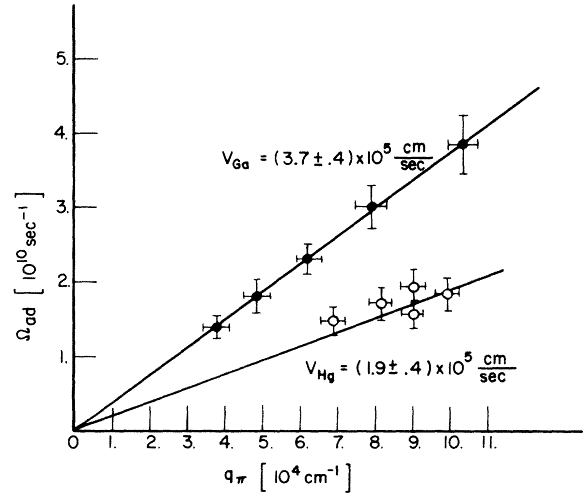

FIG. 6. Measured acoustic dispersion curves for liquid mercury and gallium; v is the velocity of sound of angular frequency Ω_{ad} and propagation constant q_π; the open circles refer to mercury, the solid circles to gallium.

The cutoff frequencies for the Brillouin spectra are determined by q_π by Eq. (4.1). By varying q_π, i.e., by varying θ_0, the $\Omega_{ad} = \Omega_{ad}(q_\pi)$ curve can be determined. It is plotted in Fig.6. A linear relation

$$\Omega_{ad} = q_\pi v\,, \quad (5.1)$$

can be deduced from the spectra taken from mercury and gallium where it is assumed that q_π corresponds to the peak maximum. The ratio of the slopes of the straight lines in Fig. 6 is given by

$$(v_{Ga}/v_{Hg}) \simeq 1.9\,, \quad (5.2)$$

and is equal to the ratio of the corresponding values determined by ultrasonic techniques. However, the present values of $v_{Hg,Ga}$ are 38% higher than the values given in the literature.[17] This discrepancy suggests that the dynamics of the fluctuations in a region close to the surface are more complicated than the simple model that is usually employed for an infinite continuum [Eq. (3.15)]. In our theory [Eq. (A5)], q_π corresponds to a peak maximum. If, instead, we had identified the minimum just before the peak with q_π, then there would be a better agreement between the sound velocities deduced in this latter way and the previous ultrasonic determinations.[17]

The number of photons per second per unit angular frequency interval scattered in the solid angle, $d\Omega \simeq 0.04$ steradians (Fig. 1), can be calculated from Eq. (3.14) combined with Eqs. (A2)-(A5). Substituting the appropriate quantities and convolving the theoretical spectrum with the instrumental profile, yields a predicted value of $\simeq 5 \times 10^{-8}$ photons at $\omega_s - \omega_0 = q_\pi v$ for scattering from mercury ($n_{Hg} = 1.4$, $\kappa_{Hg} = 4.4$, $\Gamma_{Hg} = 0.9 \times 10^{-6}$ m^2/sec). The corresponding value observed in the scattering measurements on mercury is $\simeq 7 \times 10^{-6}$ photons, suggesting that the coupling as given by Eq. (3.13) is underestimated, or the phonon distribution close to the surface is increased above that given by Eq. (3.15). Moreover, according to the theory, the spectra from gallium ($n_{Ga} = 0.89$, $\kappa_{Ga} = 5.6$, $\Gamma_{Ga} = 2.7 \times 10^{-6}$ m^2/sec) should be an order of magnitude weaker than the one from mercury although spectra of equal intensity were observed.

Finally, the line shapes of the spectra shown in Fig. 5 are compared with the predictions as expressed by Eq. (A2) combined with (A5). To this purpose, the velocities of sound and the intensities at the peaks are adjusted to their observed values in Fig. 5. For liquid mercury, the signal-to-noise ratio is too small to draw any definite conclusions about the line shape. For gallium, the long tail, which occurs when $q_\pi v \ll \omega_s - \omega_0 \lesssim 2\kappa k_s v$ (Fig. 4), should appear as a large, nearly flat, background in the center of the spectrum due to the overlapping of many orders. The actual spectrum shows a smaller background than predicted. If the damping Γ would be one or two orders of magnitude larger, the peaks at $\omega_s - \omega_0 = q_\pi v$ would broaden and the match would become better. However, the absence of the long tail remains.

The origin of these discrepancies are again thought to be the simple model employed for the calculation of $\langle |\Delta\rho_q(\omega_s - \omega_0)|^2\rangle$ in the region very close to the boundary [Eq. (3.15)]. There are two lines of inquiry which should be pursued in order to make this calculation more realistic.

The first is the investigation of phonon reflection at the interface which has been mentioned by Pine and Dresselhaus.[18] However, the present authors disagree with their model. Pine and Dresselhaus[18] employ a model in which the inelastically scattered wave inside the medium interferes with its reflection from the boundary resulting in a line shape that differs appreciably from the one presented in Sec. III and would not match our spectra. This reflected wave is used in our formulation to satisfy the electromagnetic boundary conditions. Since it does not appear outside the medium at the point of observation, it should not be included in calculating the energy spectrum at P.

The second area to be investigated is the assumption of an electronic transition region within a few monolayers of the boundary. This transition layer is presumed to introduce drastic variations in the electrical conductivity at the surface.[19]

VI. CONCLUSIONS

These observations from liquid metals have significant implications for the use of Brillouin scattering to study materials with quite general optical properties. The small penetration of the incident light is a unique probe of phonon properties within a few hundred angstroms of the metal surface. In order to analyze our spectra, we have presented a theory which seems to be a good starting point in that it describes the major features we have seen. However, the match is not perfect. We have tried not to minimize the disagreements, but rather to emphasize them so that further work can proceed to narrow the gap between theory and experiment.

ACKNOWLEDGMENTS

The authors want to express their appreciation to John R. Sandercock for advice in building the Brillouin spectrometer, and to George C. Sherman for his valuable suggestions concerning the electromagnetic boundary condition problem. Also they are very grateful to the Philips Research Laboratories which sponsored the first author during the preparation of this article and in his doctoral research.

APPENDIX

In this appendix, we describe the derivation of the lineshapes of the anti-Stokes and central components.

The conversion of the summation term in Eq. (3.14) into an integral proceeds most conveniently when we consider the anti-Stokes term in Eq. (3.15) combined with Eq. (3.14):

$$I_{\mathrm{AS}}(\omega_s - \omega_0) \equiv \sum_{q_z=0}^{\infty} \frac{\mathfrak{L}(\omega_s - \omega_0 - \Omega_{\mathrm{ad}}(q); \gamma_{\mathrm{ad}}(q))}{(q_z - 2nk_s)^2 + (2\kappa k_s)^2} . \qquad \text{(A1)}$$

Substituting the long-wavelength limits of Eq. (3.18) in Eq. (A1) and converting the summation into an integral leads, after considerable algebra, to[6]

$$I_{\mathrm{AS}}(\omega_s - \omega_0) = \frac{f(\omega_s - \omega_0)}{\Delta q_z}$$

$$\times \begin{cases} \dfrac{1}{\{[(\omega_s - \omega_0)^2 - q_\pi^2 v^2]^{1/2} - 2nk_s v\}^2 + (2\kappa k_s v)^2} \, \dfrac{v^5}{\Gamma^2} \, \dfrac{1}{(\omega_s - \omega_0)^2 + v^4/\Gamma^2} & \text{for } \omega_s - \omega_0 \geqslant q_\pi v , \qquad \text{(A2a)} \\ \dfrac{v}{(2nk_s v)^2 + (2\kappa k_s)^2} & \text{for } 0 \leqslant \omega_s - \omega_0 \leqslant q_\pi v , \qquad \text{(A2b)} \end{cases}$$

in which

$$f(\omega_s - \omega_0) \equiv \int_0^\infty \mathfrak{L}\left(q - \frac{\omega_s - \omega_0}{v} ; \frac{(\omega_s - \omega_0)^2 \Gamma}{v^3}\right) dq_z , \qquad \text{(A3)}$$

and

$$\Delta q_z = \begin{cases} 2\pi\kappa k_s & \text{for } n - \kappa \gtrsim 1 , \qquad \text{(A4a)} \\ \pi\kappa k_s & \text{for } \kappa - n \gtrsim 1 . \qquad \text{(A4b)} \end{cases}$$

The integral in Eq. (A3) can be evaluated in a straightforward manner[6] and takes the form

$$f(\delta)=\frac{1}{\sqrt{2}\,(\delta^2+d^2)^{1/4}}\begin{cases}\cos[\tfrac{1}{2}\tan^{-1}(d/\delta)] & \text{for } 0\leqslant\delta\ll 1\,, \quad \text{(A5a)}\\ \sin[\tfrac{1}{2}\tan^{-1}(d/|\delta|)] & \text{for } -1\ll\delta\leqslant 0\,, \quad \text{(A5b)}\end{cases}$$

where

$$\delta\equiv 1-q_\pi v/(\omega_s-\omega_0)\,, \qquad \text{(A6a)}$$

and

$$d\equiv q_\pi\Gamma/2v\,. \qquad \text{(A6b)}$$

The derivation of the line shape of the broadened central component proceeds in a similar way by using Eq. (3.18). It can be shown that[6]

$$I_C(\omega_s-\omega_0)=\frac{(\Delta q_z)^{-1}}{[(|\omega_s-\omega_0|/2\chi-q_\pi^2)^{1/2}+2nk_s]^2+(2\kappa k_s)^2}\times\frac{1}{5}\,\frac{(2/\chi)^{1/2}}{(|\omega_s-\omega_0|-2\chi q_\pi^2)^{1/2}}$$

$$\text{for } |\omega_s-\omega_0|\gg 2\chi q_\pi^2\,. \qquad \text{(A7)}$$

---

*Present address: Philips Research Laboratories, Eindhoven, The Netherlands.

[1] B. I. Bennett *et al.*, in *Proceedings of the Second International Conference on Light Scattering in Solids*, edited by M. Balkanski (Flammarion, Paris, 1971), p. 443

[2] B. I. Bennett *et al.*, Ann. Phys. 71, 357 (1972).

[3] J. R. Sandercock, Opt. Commun. 2, No. 2, 73 (1970).

[4] J. R. Sandercock, Phys. Rev. Lett. 28, 237 (1972).

[5] J. R. Sandercock, RCA Rev. 36, 89 (1975).

[6] J. G. Dil, Ph.D., thesis (Institute of Optics, University of Rochester, 1975) (unpublished), available in print at Philips Research Lab., Eindhoven, Netherlands.

[7] T. E. Faber *et al.*, J. Opt. Soc. Am. 58, 102 (1968).

[8] J. G. Dil, M. S. thesis (Institute of Optics, University of Rochester, 1974) (unpublished).

[9] T. E. Faber, *Introduction to the Theory of Liquid Metals* (Cambridge U.P., London, 1972), Sec. 5.22.

[10] H. N. Spector, Solid State Phys. 19, 291 (1966).

[11] J. Gasper, M.S. thesis (Institute of Optics, University of Rochester, 1972) (unpublished).

[12] J. Gasper *et al.*, J. Opt. Soc. Am. (to be published).

[13] I. L. Fabelinskii, *Molecular Scattering of Light* (Plenum, New York, 1968).

[14] D. L. Mills *et al.*, Ann. Phys. 56, 504 (1970).

[15] J. M. Stone, *Radiation and Optics* (McGraw-Hill, New York, 1963), p. 253.

[16] J. G. Dil *et al.*, in *Proceedings of the Third International Conference on Light Scattering in Solids*, edited by M. Balkanski *et al.* (Flammarion, Paris, 1975), p. 340.

[17] Landolt-Börnstein, *Molecular Acoustics* (Springer Verlag, New York, 1967), Vol. 5, p. 14.

[18] A. S. Pine *et al.*, in Ref. 16, p. 138.

[19] S. A. Rice *et al.*, Adv. Chem. Phys. 27, 453 (1974).

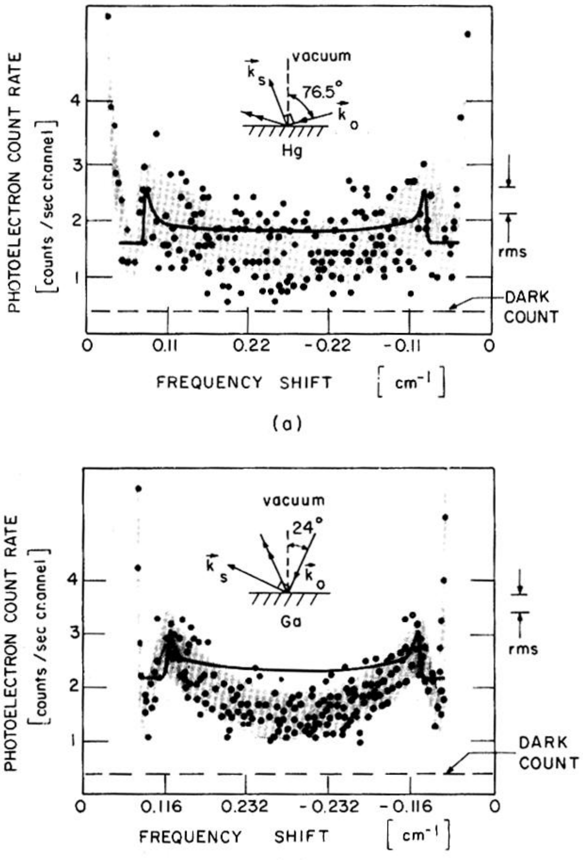

FIG. 5. Brillouin spectra from liquid mercury (a) and gallium (b); the free spectral range for Hg is 0.55 cm^{-1} = 392 channels; the free spectral range for Ga is 0.579 cm^{-1} = 400 channels. The ordinate is the absolute photoelectron count rate. The dots are the accumulated signal. The shaded area is the region within one standard deviation of a smoothed curve through the data points. The solid line is the theoretical line shape [Eqs. (A2)–(A6)] convolved with the instrumental profile.